Unsteady Aerodynamics of the Retropropulsion Reentry Burn of Vertically Landing Launchers

Ansgar Marwege* and Ali Gülhan†

DLR, German Aerospace Center, 51147 Cologne, Germany

https://doi.org/10.2514/1.A35647

During the vertical descent and landing of a launcher first stage with the aid of retropropulsion, commonly two main propulsive deceleration maneuvers are performed: the reentry burn in high altitudes at hypersonic to supersonic speeds and the landing burn shortly before touchdown at transonic to subsonic speeds. In the frame of the EU-funded H2020 project Retro Propulsion Assisted Landing Technologies (RETALT), the unsteady aerodynamics of those retropropulsion phases were studied. This paper presents results of experiments performed in the Hypersonic Wind Tunnel Cologne on the hypersonic reentry burn. The exhaust plume was simulated with pressurized air. Proper orthogonal decomposition was performed on high-speed schlieren videos, and spectral analyses of the time histories of the resulting modes were compared to the frequency content found in high-frequency pressure measurements. Dominant frequencies were found in the proper orthogonal decomposition modes for one and for three active engines. In the pressure measurements, dominant frequencies could only be observed for three active engines. The normalized pressure fluctuations are in the range of 0.002–0.012. Additionally, a good scaling of the pressures on the base area and in the wake of the configuration with the total pressure downstream of the bow shock could be confirmed, in the sense that the ratio of the local surface pressure to the total pressure downstream of the bow shock match for varying freestream Mach numbers.

Nomenclature

C_p	=	pressure coefficient
C_T	=	thrust coefficient
F_T	=	thrust
f	=	frequency
M	=	Mach number
p	=	static pressure
p'	=	pressure fluctuation
q	=	dynamic pressure
Re	=	Reynolds number
R_{mA}	=	momentum ratio
Sr_D	=	Strouhal number
u	=	velocity
ρ	=	density

Subscripts

CC	=	total condition in the wind tunnel model (CC, combustion chamber)
e	=	wind tunnel model nozzle exit condition
rms	=	root mean square
$T, 2$	=	total condition downstream of the normal portion of the bow shock
0	=	total condition in the freestream
∞	=	freestream condition

I. Introduction

RETROPROPULSION commonly means firing one or several engines against the flight direction for the deceleration of a vehicle. This technology was successfully applied by SpaceX on its Falcon 9 launcher to descend and land its first stage. In the EU H2020 project Retro Propulsion Assisted Landing Technologies (RETALT), the key technologies for the decent and vertical landing of launchers with the aid of retropropulsion were investigated. Figure 1 shows the mission concept of the RETALT1 vehicle, which is a two-stage-to-orbit vehicle with a payload of 14t to geostationary transfer orbit. Table 1 shows the main characteristics of the RETALT1 vehicle, and Fig. 2 shows its outline.

After the ascent, the main engine cutoff (MECO), and the stage separation, the first stage is recovered. In case of high payloads and high target orbits, a down range landing (DRL) is performed on a seagoing platform. The first stage is decelerated at high altitudes with three engines to limit heat loads and the dynamic pressure in the following aerodynamic phase. This first hypersonic retropropulsion maneuver is called the reentry burn. Then, the vehicle is decelerated a second time shortly before touchdown. This subsonic retropropulsion maneuver is called the landing burn. For smaller payloads, the stage can be landed close to the launch site, which is the return to launch site (RTLS) scenario. It differs from the DRL scenario in the additional boostback burn that is performed to bring the stage back to the launch site.

The aerodynamics of the various flight phases were investigated with the aid of extensive wind tunnel experiments. The reentry burn was simulated in the Hypersonic Wind Tunnel Cologne (H2K) [1,2], the aerodynamic phase was studied in the Trisonic Wind Tunnel Cologne (TMK) [2,3], and the landing burn was tested in the Vertical Free-Jet Facility Cologne (VMK) [2].

This paper focuses on the investigation of the hypersonic retropropulsion maneuver at the reentry burn. Even though, in [1], detailed analyses of the hypersonic retropropulsion flowfield were performed, a dedicated modal and frequency analysis was not performed. High-frequency pressure loads can damage structures and actuators and can lead to a system failure [4,5], and are, hence, critical for the design of launch systems. Therefore, the aim of the work at hand is a detailed modal and frequency analysis of the unsteady flowfield during the hypersonic reentry burn.

The paper is structured as follows. First, a short overview of the state-of-the-art in supersonic and hypersonic retropropulsion is given. Then, the experimental setup, the wind tunnel, the model, and the instrumentation are laid out. This is followed by the description of the test conditions. Finally, the results of a detailed modal and frequency analysis of the schlieren recordings and high-frequency pressure measurements are discussed. The paper is closed with conclusions and an outlook. A complementary analysis of the unsteady aerodynamics of the subsonic landing burn can be found in [6].

*Research Scientist, Supersonic and Hypersonic Technology Department, Institute of Aerodynamics and Flow Technology; ansgar.marwege@dlr.de.

†Head of Department, Supersonic and Hypersonic Technology Department, Institute of Aerodynamics and Flow Technology; ali.guelhan@dlr.de.
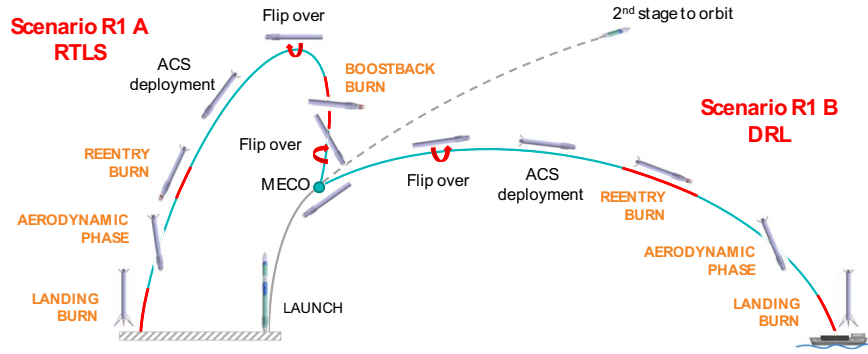
Fig. 1   RETALT1 mission concept (adapted from [7]).

Table 1   Main characteristics of the RETALT1 configuration as presented in [8]

| Stage characteristic	1st stage	2nd stage	Fairing	Total
Number of engines	9	1.0		10.0
Reusability	+	±	−	±
Height, m	71.2	19.8	12.0	103.0
Diameter, m	6.00	6.00		6.00
Mass full (gross lift-off weight), t (including payload)	680.8	204.2	2.5	899.0
Stage rate, %	75.7	24.3		
Structure coefficient, %	8.7	8.3		
Mass structure, t	59.3	16.7		75.9
Propellant mass (including descent propellant), t	621.5	187.5		809.0
Descent propellant, t	50.0	0		50.0
Propellant reserve and residuals mass, t	7.500	2.500		10.0
Engines	RETALT1-LHLOX-E15-FS	RETALT1-LHLOX-E70-FS		
Engine cycle	Gas generator	Gas generator		
Oxidizer/propellant	LOX/LH2	LOX/LH2		
Expansion ratio	15	70		
Specific impulse sea level, s	372.2	294.4		
Specific impulse vacuum, s	401.6	431.9		
Thrust sea level, kN	$9 \times 1179 = 10{,}614$	$1 \times 930 = 930$		
Thrust vacuum, kN	$9 \times 1273 = 11{,}453$	$1 \times 1364 = 1364$		
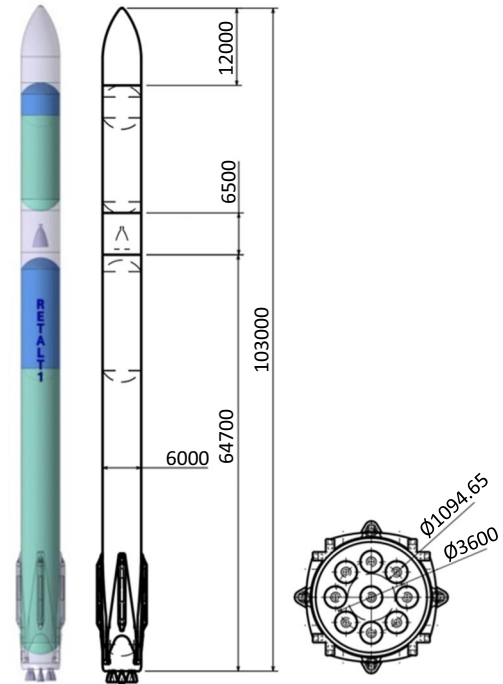
Fig. 2   Outline of the RETALT1 configuration (adapted from [8]) (dimensions in millimeters).

II.   Supersonic and Hypersonic Retropropulsion

Supersonic retropropulsion (SRP) commonly refers to the direction of a supersonic jet against a supersonic freestream. These flowfields have been studied since the 1950s for entry, descent, and landing (EDL) applications [9]. The recent research in the USA foremostly concentrates on EDL missions for Mars [10–20]. Analytical approaches to model these flows have been developed by Korzun and Braun [21] and Cordell and Braun [22] based on Finley [23] and Jarvinen and Adams [24]. The status of the Mars EDL research is summarized in [17]. Only some studies were published on launchers in the USA, e.g., [10]. In contrast, the research in Europe focuses on the descent and vertical landing of launcher first stages [1–3,25–33]. The phenomena for these two applications are generally very similar, with the difference that the launcher first stages are more slender and the vehicles for Mars EDL commonly have a much larger cross-surface area compared to the engine exit area. Furthermore, the mission profiles differ and the aerodynamic thrust coefficients for the vertical landing launchers are much larger. Also motivation exists in Europe and in India to adapt this technology to aerospike engines [34–36]. Comprehensive literature reviews of investigations in supersonic retropropulsion can be found by Korzun et al. [9] and Mejia and Schmidt [37], where Mejia and Schmidt [37] link the research

performed on SRP to research performed on stagnation point injection (SPI), in which some findings made in SRP were discovered in parallel. A review of research in SPI can be found in [38].

SRP flowfields for a single active engine commonly appear in two flow modes, the so-called blunt mode (Fig. 3) and a long penetration mode (Fig. 4) [24,39].

In the case of the blunt mode the flow is composed of two components: the strongly underexpanded plume of the supersonic jet, and the bow shock of the freestream. These two flowfields meet at the contact surface. In the highly underexpanded plume the flow is strongly expanded around the lip of the nozzle exit and is then recompressed and redirected toward the symmetry axis. In this case the barrel shock is very close to the jet boundary. For high thrust coefficients, the Mach disc in the retropropulsion flows can get strongly bent and exhibits a spherical shape. Also the reflection of the barrel shock on the Mach disc is visible. In the wake of the plume a recirculation zone forms. The incoming freestream is decelerated through the bow shock to subsonic speeds. It is then accelerated along the contact surface to supersonic speeds again.

As the pressure surrounding the nozzle exit is not the ambient pressure in these flowfields but the dead air pressure p_d present in the recirculation zone, the plume expansion in this case is dominated by the exit pressure ratio (EPR) defined as [40]
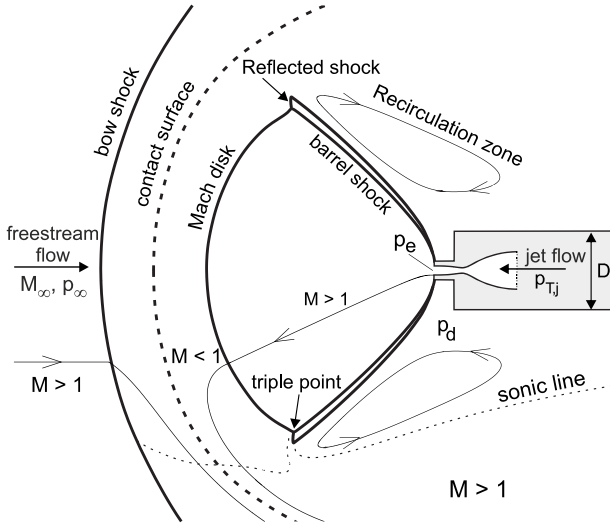
$$\text{EPR} = \frac{p_e}{p_d} \tag{1}$$

Fig. 3 Flow features of the blunt mode of a supersonic or hypersonic retropropulsion flowfield for the single-engine case (adapted from [40]).
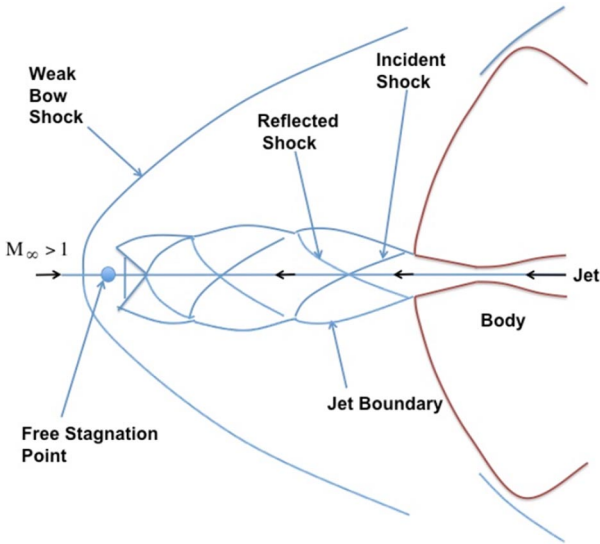

Fig. 4 Flow features of the long penetration mode of a supersonic or hypersonic retropropulsion flowfield for the single-engine case (reprinted from [39]).

where p_e is the nozzle exit pressure. One of the challenges for supersonic retropropulsion flowfields remains in the determination of the dead air pressure in the recirculation zone as it cannot be assessed analytically [40]. Therefore, Korzun and Cassel [11] proposed the use of the ratio of the exit pressure p_e to the total pressure downstream of the normal portion of the bow shock $p_{0,2}$ as scaling parameter. Gutsche et al. [40] then proposed to also scale the surface pressures with $p_{0,2}$ instead of using the conventional pressure coefficient C_p for these flowfields. It was shown in computational fluid dynamics (CFD) simulations that this leads to better similarity for varying Mach numbers, at least in the base area close to the plume [40].

The flowfield features of the blunt mode (bow shock stand-off distance, Mach disc location, location of the triple point) were found to be dependent on the square root of the aerodynamic thrust coefficient [24,40], which is defined as follows:

$$C_T = \frac{F_T}{q_\infty A_{\text{ref}}} \quad (2)$$

with the thrust F_T, the dynamic pressure q_∞, and a reference area based on the body diameter A_{ref}. Interchangeably, for the aerodynamic thrust coefficient, also the momentum ratio R_{mA} can be used as similarity parameter [37]:

$$C_T = \frac{F_T}{q_\infty A_{\text{ref}}} = \frac{\rho_e u_e^2 A_e}{1/2 \rho_\infty u_\infty^2 A_{\text{ref}}} = 2R_{\text{mA}} \quad (3)$$

where ρ_e and u_e are the density and the velocity at the nozzle exit with an area of A_e, and ρ_∞ and u_∞ are the density and velocity in the freestream. Equally C_T can be rewritten in terms of the momentum flux ratio, $\text{MFR} = (\rho_e u_e^2)/(\rho_\infty u_\infty^2)$:

$$C_T = 2\text{MFR} \frac{A_e}{A_{\text{ref}}} \quad (4)$$

This connects SRP flows with subsonic retropropulsion flows where the MFR is used as similarity parameter [41].

It shall be noted that the thrust coefficient, R_{mA}, and MFR can only be used interchangeably if the pressure loss in the thrust is neglected.

The long penetration mode is shown in Fig. 4. Instead of the highly underexpanded plume structure, here a jet train with several shock cells is formed, which ultimately terminates in a normal shock. In experiments, this clear shock train structure is not always observable and the flow is highly unsteady [24].

The condition for the switching of one to the other mode is still under discussion in the SRP community. Jarvinen and Adams [24] theorized that it depends on a certain ratio of exit pressure to ambient pressure (p_e/p_∞), and it appears at thrust coefficients close to unity. Korzun and Cassel [11] argued that the switch appears at $C_T > 1$ and ($p_e/p_{0,2}) > 1$. Daso et al. [42] and Gutsche et al. [40] postulated that the switch could appear when the nozzle exit flow changes from being underexpanded to being overexpanded and, therefore, would depend on the EPR. Furthermore, Gutsche et al. [40] theorized that the dead air pressure depends on the base geometry, which is why also the ratio of $p_e/p_{0,2}$ at which the modes switch depends on the geometry. The theory of the mode switch depending on weather the nozzle exit flow is under- or overexpanded is in contradiction to Venkatachari et al. [39], where the long penetration mode was found for underexpanded jets. Hence, it can be summarized that the main parameters for the switch between the modes seem to be the ratio $p_e/p_{0,2}$, the EPR, and the thrust coefficient. What is commonly agreed on in the SRP literature is that the switch between blunt and long penetration mode appears at low thrust coefficients [11,24,40].

In [1,43] the term "hypersonic retropropulsion" (HRP) was used instead of SRP as the Mach numbers tested in the H2K were above 5. The general flowfield was, however, comparable to the SRP flowfield features. In [1], the flow features for three active engines in one plane could also be shown to depend on the square root of the thrust coefficient. The blunt and long penetration modes for three active engines in the alpha plane are shown in Figs. 5 and 6. Vos et al. [28] studied the flowfield with three active engines in the alpha plane in more detail and varied the heat capacity ratio to assess its influence on the plume shape showing that it is an important parameter for the extrapolation from wind tunnel experiments to flight conditions. The pressure on the base area of the vehicle is known to decrease with
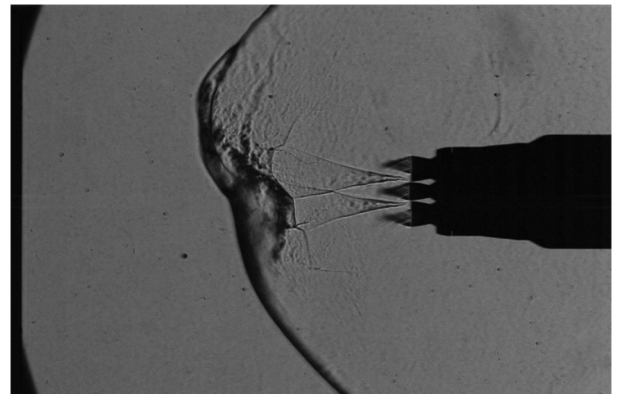

Fig. 5 Instantaneous schlieren image of blunt mode for three active engines in the alpha-plane at an angle of attack of $0°$ (reprinted from [1]).
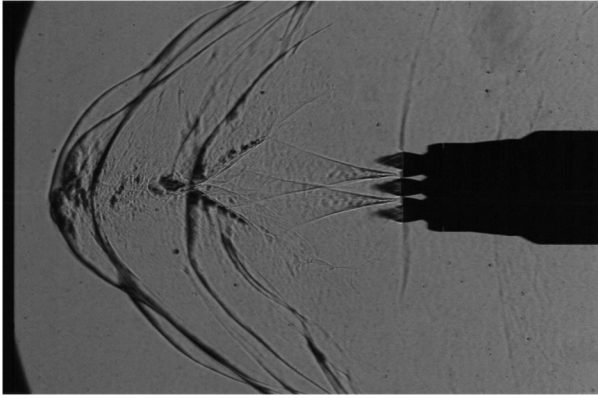
Fig. 6   Instantaneous schlieren image of long penetration mode for three active engines in the alpha-plane at an angle of attack of 0° (reprinted from [1]).

increasing thrust coefficient [1,11,24,40], which leads to a decrease in the drag coefficient with increasing thrust coefficient [41,44].

The flowfield of the blunt mode of SRP flowfields is in general steady, where the strongest unsteady behavior is found in the triple point [45]. To characterize the dynamic flow features of the blunt mode of SRP flowfields, experimental data were studied in detail by Bathel et al. [46] by means of spectral images and proper orthogonal decomposition (POD). They found a fundamental frequency of 2 kHz. In [37] a POD of experimental data was performed, which was combined with a spectral analysis of measured axial forces, and a fundamental frequency of 4.2 kHz was found to be associated with the flow motion. In [43] a spectral analysis of similar experimental schlieren videos was presented and was linked to high-frequency pressure measurements. A dependence of the dominant frequency on the freestream Mach number was shown. Spectral analyses of resulting aerodynamic forces obtained with CFD have been presented by Montgomery et al. [47] and Chen el al. [48]. Chen et al. [48] went into further detail and linked the POD and spectral analyses and proposed a feedback model for the blunt and the long penetration mode. Chen et al. [48] found dominant frequencies at Strouhal numbers of 0.252 and 1.506.

Schauerhamer et al. [49] described a feedback mechanism for the unsteadiness of the blunt mode for a single nozzle case. Oscillations in the triple point generate pressure waves that propagate to the bow shock, generating small changes in the flowfield of the incoming freestream. These effects then propagate down to the

vehicle surface, where they are reflected and affect the pressure in the recirculation zone, which in turn affects the EPR. The caused fluctuations in the EPR then close the feedback cycle by affecting the oscillation in the triple point. Codoni and Berry [50] analyzed the power spectral density (PSD) of pressure measurements performed in wind tunnel experiments of the same configuration as described in [49]. They found distinctive frequency peaks, which are especially pronounced for an angle of attack of 0° and which weaken for higher angles of attack. They also analyzed configurations with three active engines, which were found to show less pronounced frequency peaks. In [43] surface pressures on the cylindrical part of a launcher configuration were analyzed for a single-engine case and dominant frequencies were shown to increase with increasing angle of attack in this region.

III.   Experimental Setup

A.   Hypersonic Wind Tunnel Cologne

As stated in the Introduction, the reentry burn of RETALT1 was tested in the H2K, where the exhaust plume was simulated with compressed air. A scheme of the H2K is shown in Fig. 7.

H2K is a blowdown facility. Compressed air up to 60 bar passes an electrical heater and a settling chamber and is accelerated through a Laval nozzle to supersonic or hypersonic speeds. After the test chamber, the flow is decelerated in a diffusor before entering the vacuum chamber. The Mach numbers are varied by exchanging the Laval nozzle. Mach numbers of 4.8, 5.3, 6.0, 7.0, 8.7, and 11.2 can be tested. By a variation of the total pressure and total temperature, the unit Reynolds number can be varied in a range of 2.0×10^6 m^{-1} to 20.0×10^6 m^{-1}. With the electric heaters a maximum power of 5 MW, stagnation temperatures of up to 1000 K can be reached. The common test duration is about 30 s. Quartz glass windows give visual access to the test chamber, such that schlieren recordings can be performed. The facility is described in more detail in [51].

B.   Wind Tunnel Model and Instrumentation

The model setup for the H2K facility was already described in [1] and is shortly summarized here. A schematic of the RETALT1 model is shown in Fig. 8, and the wind tunnel model mounted in the H2K facility is shown in Fig. 9. The model is designed such that a short and a long version of the model can be tested by adding or removing the cylindrical segment shown in Fig. 8. While the long model version is used for force measurements, the short model version is intended for detailed analyses of the base flow using high-frequency pressure measurements. In this
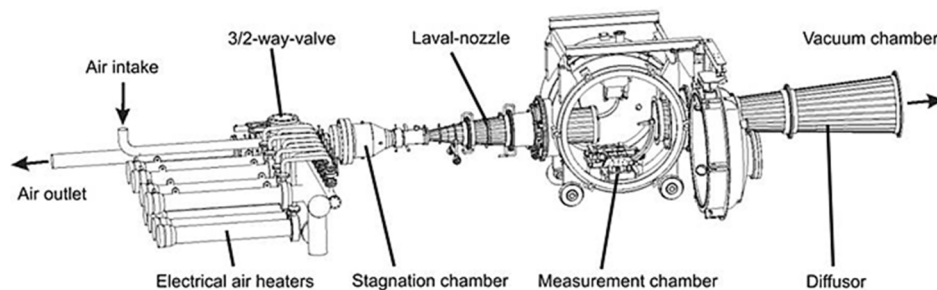

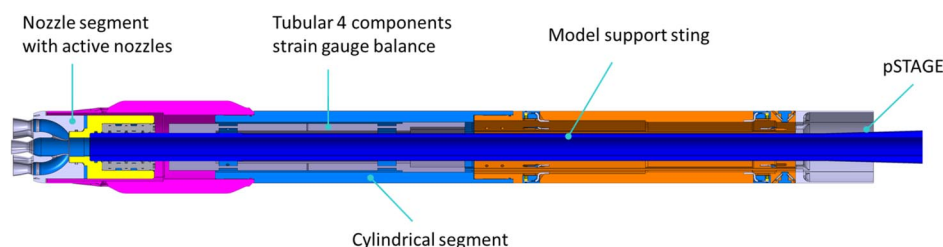**Fig. 7   Scheme of the Hypersonic Wind Tunnel Cologne (H2K).**

Fig. 8   RETALT1 wind tunnel model design (reprinted from [1]).

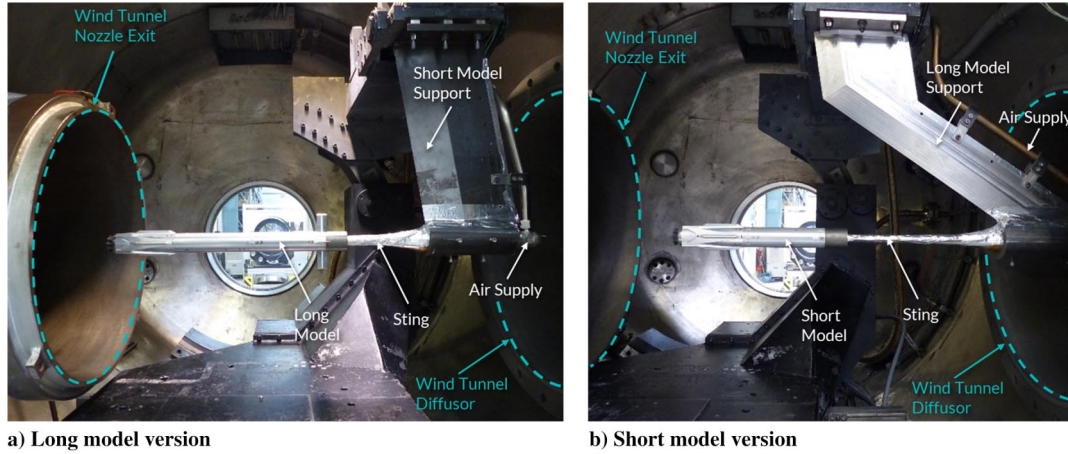**a) Long model version**   **b) Short model version**

Fig. 9   RETALT1 wind tunnel model mounted in H2K (reprinted from [1]).

paper, only results obtained with the short model are discussed. The model is scaled by 1/130 with respect to the RETALT1 flight configuration. The reference length for the nondimensionalization is the diameter of 6 m in the flight configuration (hence 46.154 mm in the experiment). The reference area is the base area A_B of 28.27 m^2 for the flight vehicle. For the simulation of the exhaust plume, air is blown out through a hollow model support sting and a model nozzle (see Fig. 8). Various nozzle segments were manufactured for tests with different engine combinations, i.e., one active engine or three active engines, and different engine deflection angles. The locations of the high-frequency pressure sensors are shown in Fig. 10. The pressure sensors are distributed in three measurement planes. One close to the interstage (plane 1), one close to the folded landing legs (plane 2), and one at the model base (plane 3). Furthermore, the sensors are numbered in the clockwise direction, when looking at the base of the model. This is represented by the second index. The third index for the sensors on the base plane defines the radial positioning from a position close to the center with index 1 to the outermost sensor with index 3. The pressure in the wake was measured with a pressure tube (pSTAGE). The pressures in plane 1 and 2 were measured with LQ-062-0.7BARA Kulite pressure sensors, and the pressures in plane 3 were measured with XCQ-080-0.7BARA pressure sensors.

The model nozzles are shown in more detail in Fig. 11. They are designed with an expansion area ratio of 2.5, resulting in an exit Mach number of 2.443, with a throat diameter of 5.3 mm, an exit diameter of 8.42 mm, and an exit angle of 5.57°. The contour was designed as parabolic approximation of a bell nozzle with a fixed expansion area ratio and a fixed nozzle exit angle. The exit angle was chosen to be 5.57° to match the nozzle exit angle of the RETALT1 first-stage engine that has a thrust-optimized contour with an area expansion ratio of 15.
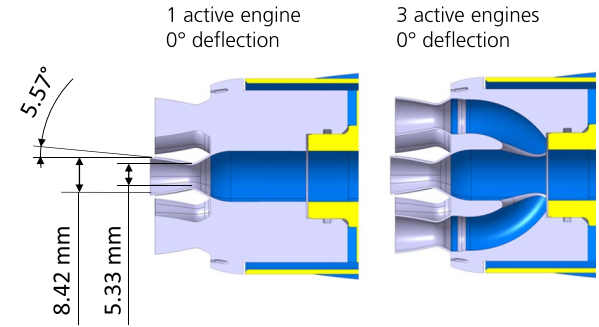

Fig. 11   Details of inner flow contour (adapted from [1]).

A detailed discussion on the chosen expansion area ratio of 2.5 for the nozzles can be found in [1].

High-speed schlieren videos were recorded with a FASCAM SA-X2 high-speed camera at 20 kHz with an exposure time of 2.5 μs. A Z-type schlieren setup with a focal length of 6 m and mirror diameter of 600 mm was used as described in [4]. The high-frequency pressure measurements were performed at 50 kHz.

IV.   Test Conditions

Figure 12 shows the reference trajectory presented in [8] mapped on the wind tunnel facilities where the tests were performed. It can be seen that the wind tunnels are well suited to rebuild the reference trajectory. In addition to the tests discussed in this paper, also the tests performed in the TMK [2,3] and the tests performed in the VMK [2] are shown. The conditions of the H2K tests discussed in this paper are
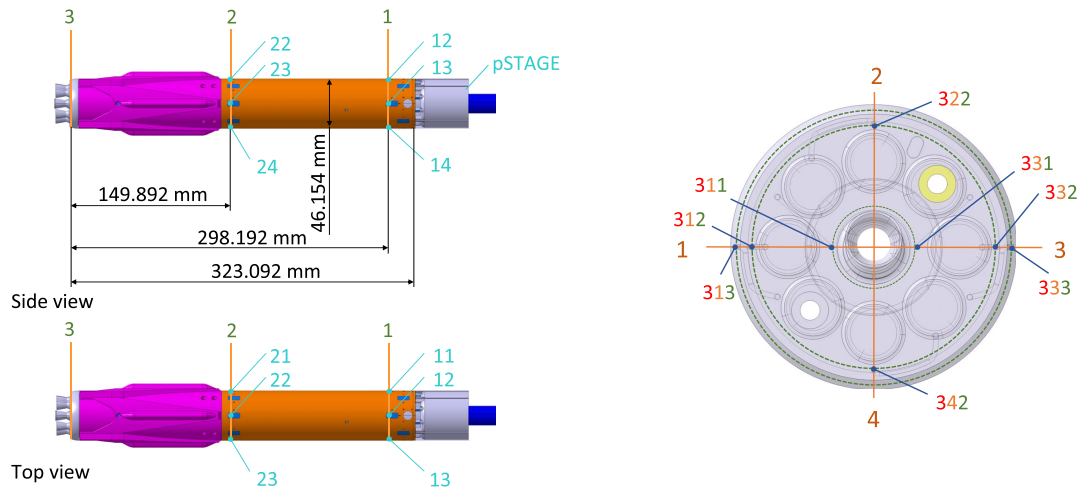

Fig. 10   RETALT1 distribution of pressure sensors (adapted from [1]).
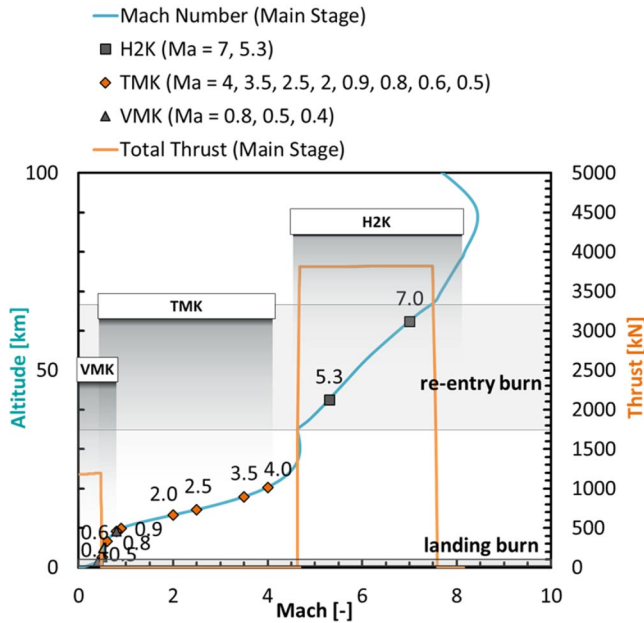
Fig. 12   Mapping of Mach numbers tested in the wind tunnel facilities at DLR in Cologne over the reference trajectory presented in [8] (adapted from [1]).

Fig. 13   Hypersonic retropropulsion flowfield for a single engine for cold (upper part) and heated air (lower part) (reprinted from [1]).

Fig. 14   Hypersonic retropropulsion flowfield for three active engines for cold (upper part) and heated air (lower part) (reprinted from [1]).

summarized in Table 2. The measured pressures and the normalized pressure fluctuations are summarized in Tables A1 and A2 in the Appendix. The thrust coefficient for the single-engine case discussed in this paper was chose to be 3.7 to be close to the maximum thrust coefficient that could be tested without a disturbance of the wind tunnel freestream due to blockage, which is 3.8 [1]. The thrust coefficient for the three-engine case was chosen to around 2.3 even though thrust coefficients up to 7.2 could be tested [1], as the main flow features were well visible in the schlieren window for this condition.

V.   Results

In this section, the steady and unsteady flow features of the hypersonic retropropulsion flowfield are analyzed. In Fig. 13 the flowfield is shown for the case with one single active engine, for cold and heated air, which was used to simulate the engine plume. As stated in [1], the flow features are similar for both cases. In Fig. 14, the flowfield for three active engines in the angle of attack plane is shown. Also here, the flowfield can be observed to be very comparable between the cold and the heated case [1].

At the stagnation point between the freestream and the jet plume, the total pressure of the freestream and that of the jet are equal [11,40]. For the single-engine case, applying this condition, the flow properties along the center line can be computed analytically. As the total pressure drop over the bow shock is known, the total pressure in the stagnation point is known. Hence, with the known total pressure in the stagnation point and in the wind tunnel model, the Mach number upstream of the Mach disc can be computed iteratively. Figure 15 shows the calculated flow properties for the single-engine case for cold and heated air for specific points on the centerline. From the freestream side, point 1 is upstream of the bow shock and 2 downstream of it, and 0,2 is the stagnation point from the freestream
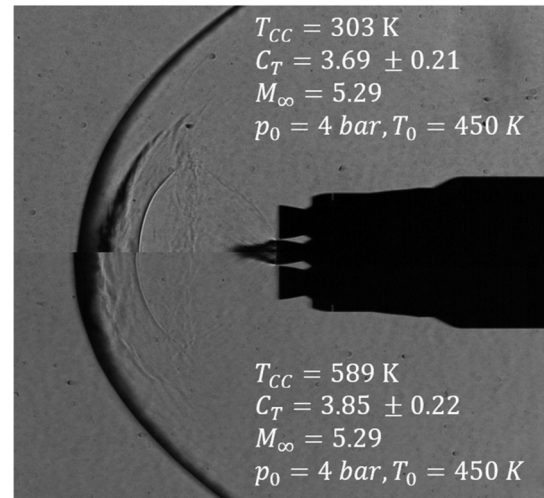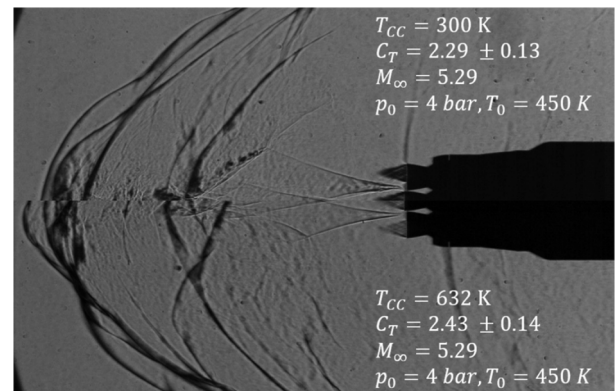
side. From the jet side, 1j is upstream of the Mach disc and 2j downstream of it, and 0,2j is the stagnation point from the jet side.

Assuming a constant heat capacity ratio, we can find that the ratios of the density and the temperatures over the shocks and due to isentropic acceleration or decelerations only depend on the Mach numbers. The Mach number on the centerline is equal in both cases; hence also the ratios between the points, 1, 2, and 0,2 on the free-stream side and 1j, 2j, and 0,2j on the jet side are equal. However, due to the higher temperatures in the heated air case, the same ratios lead to higher gradients in the temperature for the same Mach numbers. In turn, lower densities lead to lower density gradients. This is why in Fig. 13 the Mach disc is less clearly visible in the heated air case. Furthermore, it can be noted that the gradient in the contact point (between 0,2 and 0,2j) is positive in the cold case, leading to a dark appearance of the contact surface, while it is negative in the heated air case, which leads to a white appearance. Hence, the flowfield appearance changes, due to the heating. However, the Mach number, the pressures, and the momentum flux on the centerline are not affected by the temperature increase as can be seen in Fig. 15. As these quantities are the main drivers for the similarity of the flowfield,

Table 2   Test conditions of hypersonic retropropulsion tests in H2K presented in this paper

| Run	No. of engines	M_∞	C_T	MFR[a]	T_{CC}, K	Re	q_∞, bar	p_∞, bar	u_∞, m/s	ρ_∞, kg/m³	p_e, bar	u_e, m/s	ρ_e, kg/m³	$p_{T,2}$, bar
90_5	1	5.29	3.69	49.55	303	2.43E+05	0.1076	0.005	871.858	0.0283	1.276	138.225	138.225	0.20041
93_7	3	5.29	2.29	30.76	300	2.40E+05	0.1061	0.005	872.238	0.0279	0.781	136.643	136.643	0.19758
115_2	1	5.29	3.85	51.67	589	2.38E+05	0.1049	0.005	870.959	0.0277	1.297	268.524	268.524	0.19539
117_2	3	5.29	2.43	32.65	632	2.55E+05	0.1044	0.005	850.194	0.0289	0.816	288.302	288.302	0.19449

[a]MFR, momentum flux ratio
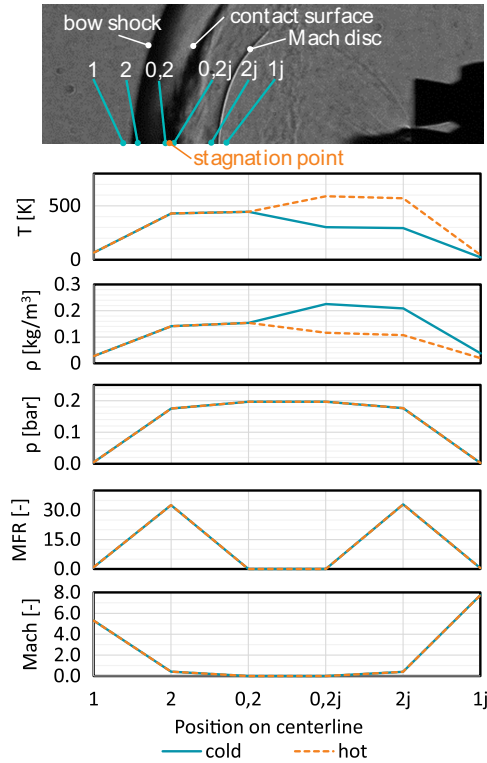
Fig. 15　Analytically calculated flow properties at selected points on the centerline for the single-engine case for cold and heated air.

the main flowfield features (bow shock stand-off distance, Mach disc location, location of the triple point) are not changed by increasing the temperature of the air.

For the hypersonic retropropulsion cases, a POD was performed over 4000 frames. It results in spatial and temporal eigenmodes ordered by their energy content. The high-speed schlieren were recorded at a frame rate of 20 kHz. Figure 16 shows the first 12 modes and several higher modes for the cold gas single-engine case. As the mean image was not subtracted from each frame, the zeroth mode shows the steady flow features. The first two modes are axisymmetric, while higher modes do not show any symmetry anymore. The reason for the asymmetry in the modes could be the vortex rings emerging from the Mach disc as described in [1], as these strongly alter the flowfield but do not appear in a symmetrical manner. The lower modes reflect mainly the oscillations in the contact surface and the associated oscillations of the bow shock. In the higher modes (mode 200 and mode 500), also the oscillations in the triple point are reflected. The feedback mechanism for the unsteadiness of the flowfield for the blunt mode described in [49] (see Sec. II) can be observed in these modes. The oscillations in the triple point generate pressure waves affecting the bow shock, which feeds back to the EPR. The EPR, in turn, affects the plume shape closing the loop by influencing the oscillations in the triple point. In Fig. 17 the singular values of the POD are shown. Figure 18 shows the cumulative energy (sum of singular values up to the current one, divided by the sum of all singular values). It can be seen that a large number of modes is necessary to capture the energy of the flow. For example, over 2000 modes (of 4000) are needed to capture 80% of the energy.

The first three modes and the zeroth mode of the corresponding case with heated air are shown in Fig. 19. Due to differing densities in the plume caused by the heating of the jet, the schlieren images have a slightly different appearance as explained above. However, in general, similar modes can be observed. Also the singular values and the cumulative energy of the modes are similar to the cold gas case (see Figs. 17 and 18).

In Fig. 20, the first 12 modes of the three-engine case are shown for cold and for heated air. The interaction of the jet with the freestream and the resulting unsteady loads on the model lead to a slight oscillatory movement of the model. These energies are captured in modes 2 and 3 in the cold gas case and in mode 1 in the heated case.

As already assumed in previous work [1,2], the most energetic mode is the switch mode between blunt and long penetration mode for both the cold gas and the heated air case (neglecting the modes that cover the oscillation of the model). This can be clearly seen in Fig. 21, comparing the first mode of the cold gas case with the variance over 10 images of the long penetration mode and of the blunt mode, used in [2] to visualize the unsteady nature of both modes. Figure 22 shows the time histories of the switching mode for the cold gas and the heated air case, where positive values correspond to the long penetration mode and negative values correspond to the blunt mode. It can be observed that, for the cold case, the change between the modes appears more abruptly, while it appears more smoothly for the heated air case. In both cases the blunt mode only appears for short time intervals. This is even more clearly visible for the cold case.

Comparing the cold gas case and the heated air case it can be observed that they slightly differ from each other. For the cold gas case the plume–plume interaction seems to play a larger role, as the unsteady oblique shocks terminating the plumes are clearly visible in several modes, e.g., modes 4, 9, 10, and 11. For the heated air, the energy seems to be more strongly related to an axial movement of the plume structure, which is, e.g., prominent in mode 7. In Fig. 23 an average modal solution for both cases is shown. It basically represents a merged solution of several modes averaged over time. Here the zeroth mode was excluded, and the time histories of the modes 1–500 were averaged over time. The spatial mode was then reconstructed from the original image snapshots. More details on the procedure for the construction of the average modal solution can be found in [6].

While the heated air flowfield is dominated by the switch between the blunt and the long penetration mode, the cold gas case is dominated by the sideways motion of the plume. The differences in the modes could come from an influence of the higher exit velocity at the nozzle exits due to the higher temperatures, higher viscosities, and a temperature effect on the heat capacity ratio. It could also partly come from the varying density gradients in flowfield due to the varied temperatures in the jets, which influences the visibility of the flow features in the schlieren images as discussed above.

As shown in Fig. 16 the drop of the singular values over the first modes is lower for the three-engine cases than for the single-engine cases. Hence, the increase of the cumulative energy over the first modes is slower as shown in Fig. 19. This is reasonable, as the unsteadiness of the flowfield in the three-engine case is a lot stronger. Therefore, more modes are necessary to capture the energy of the flowfield. The singular values and the cumulative energy of the cold and the heated air cases of the three-engine cases are very similar.

To analyze the frequency content of the POD modes, the PSD of the time series of the POD modes was computed with a short-time Fourier transform that was computed over 4000 time steps. It was performed with a Hann window with a length of 500 with a step size of 8 time steps between single spectra. The spectra were then averaged over the time steps. The frequency was resolved with 2048 bins. The Strouhal number Sr_D, which represents the normalized frequency, is defined as

$$Sr_D = \frac{f D_{\mathrm{ref}}}{u_\infty} \tag{5}$$

where f is the frequency, u_∞ is the freestream velocity, and D_{ref} is the reference length. D_{ref} was chosen to be the base diameter of the model as this makes the Strouhal numbers comparable to results of studies on near-wake flows in the base area of (ascending) launch vehicles, where this definition was used [52].

In Fig. 24, the PSDs of the first 12 modes are shown for the four hypersonic retropropulsion cases. For the cold gas case, dominant frequencies can be observed at Strouhal numbers of 0.09 and 0.082 for the single-engine case and the three-engine case, respectively. For the tests with heated air, these frequencies are slightly shifted to higher values of 0.126 and 0.141. In general, the observed frequencies are a lot less prominent than in the subsonic retropropulsion cases that are presented in [6].

In Fig. 25, the PSD of the high-frequency pressure sensors in the base area and along the cylindrical body of the model is shown for the cold gas case for one and three active engines, where the mean value
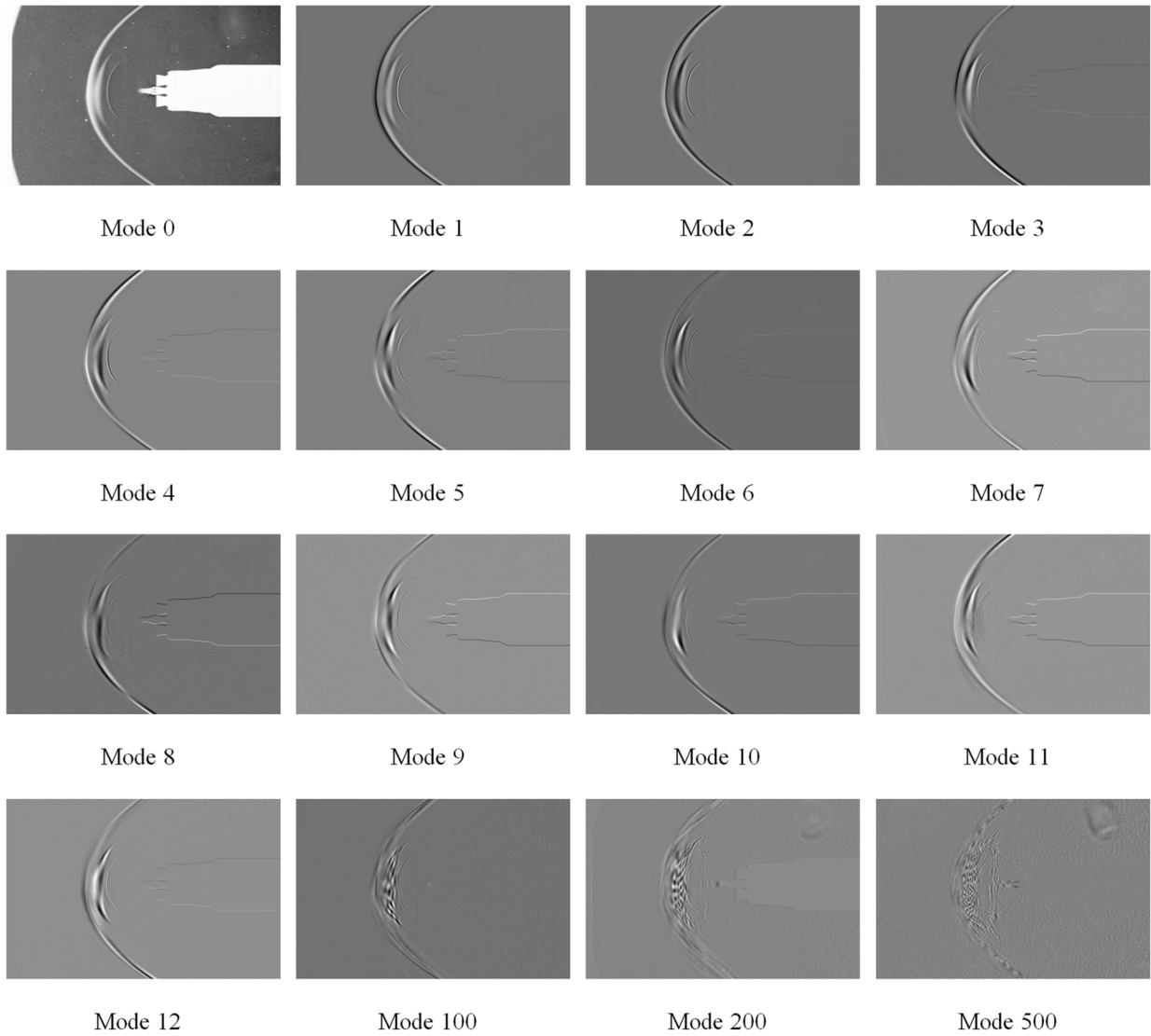
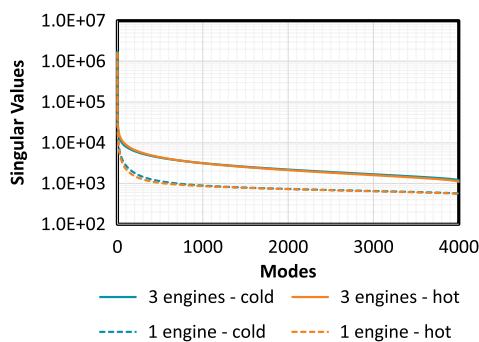**Fig. 16   POD modes of single-engine cold gas case.**

Fig. 17   Singular values of the PODs of the cold and heated air, single-engine and three-engine cases.

Fig. 18   Cumulative energies of the PODs of the cold and heated air, single-engine and three-engine cases.

was subtracted before the PSD was performed. The PSD was performed over 20,000 time steps with a Hann window of a width of 500 with a step size of 39 samples between the spectra. The frequency resolution was again 2048 bins. In general, the distribution of the frequencies is similar for both cases. The sensors are clustered by the plane they are in. The sensors 313 and 332, which are on the outer circle of the base and not in the alpha plane, show a slightly different behavior in comparison to the other sensors in plane 3. Dominant frequencies can be observed for the three-engine case. However, they cannot be observed in the single-engine case. There could be three reasons for this behavior:
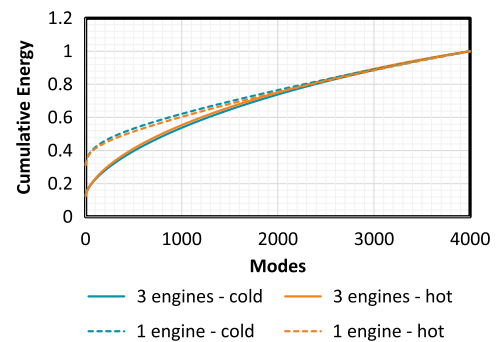
1) The frequencies could come from a buffeting phenomenon in the base area, and in the single-engine case the blunt plume shields the base area better from the incoming freestream and, therefore, mitigates those frequencies.

2) The frequencies could come from the unsteady fluctuations of the plume that are only appearing in the three-engine case.

3) As can be seen in Fig. 11 the supply lines of the outer nozzles show a sharp edge where they meet the main supply line. This causes unsteady flow separations and recirculation regions, which were observed in CFD simulations performed on the flowfield in the model.
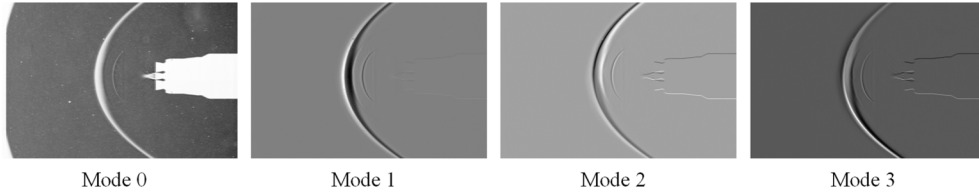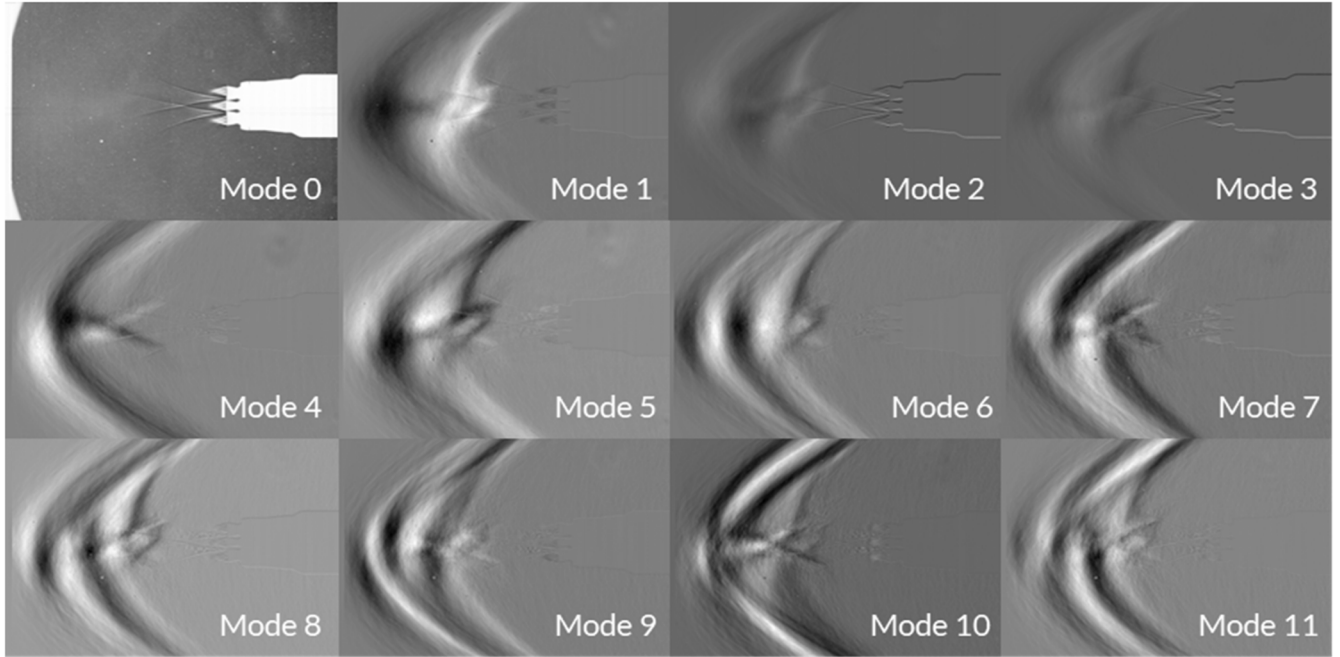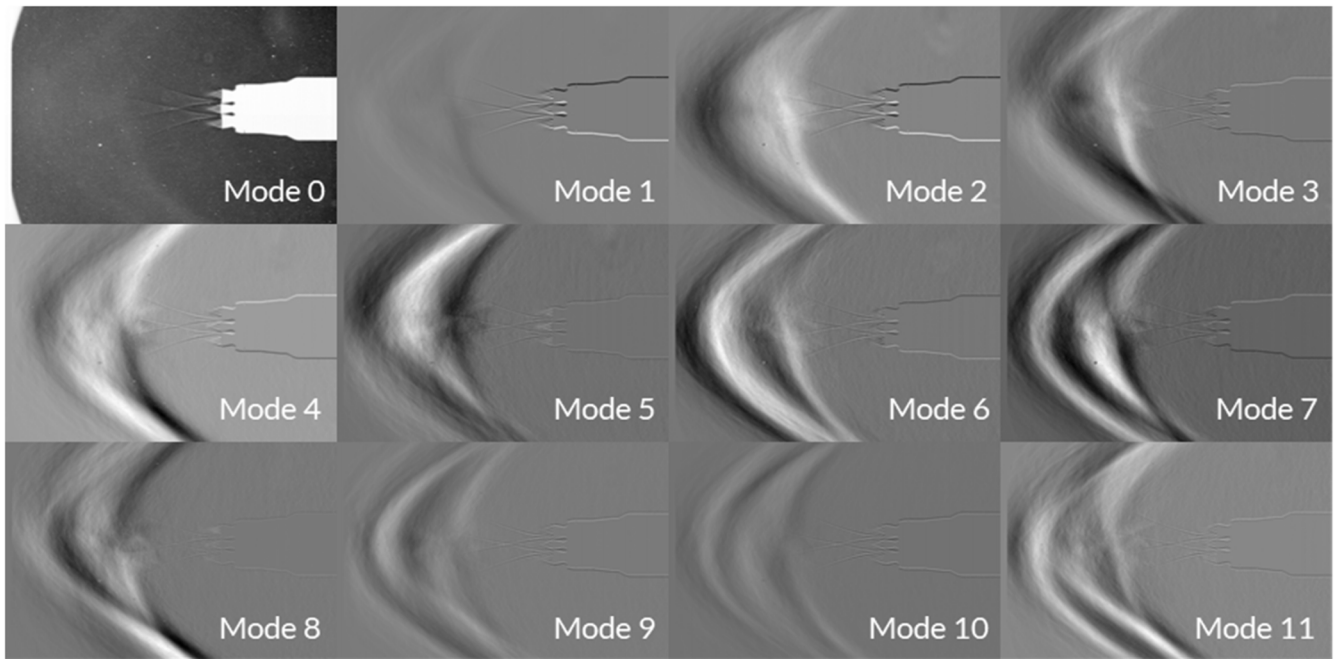
Fig. 19 POD modes of single-engine case with heated air.

a) Cold gas

b) Heated air

Fig. 20 First 12 POD modes of the three-engine case.

In [2], the dominant frequencies for the cold gas case with three engines were plotted against the thrust coefficient for the pressure sensors 311 and 331. In Fig. 26 for the same case the Strouhal number is plotted versus the thrust coefficient. It can be observed that the dominant Strouhal numbers of 1.12, 1.16, 1.19, and 1.3 appear for a large range of thrust coefficients in the pressure measurements. This is a strong indicator that they do not originate in the outer flow interactions, but from the supply line. In future
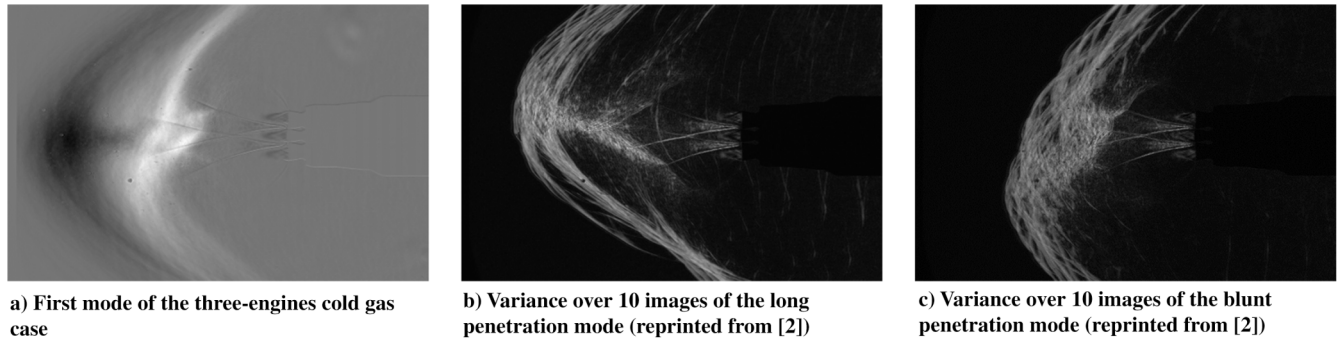
a) First mode of the three-engines cold gas case

b) Variance over 10 images of the long penetration mode (reprinted from [2])

c) Variance over 10 images of the blunt penetration mode (reprinted from [2])

Fig. 21 Comparison of first mode of the three-engine cold gas case with the visualization with the variance over 10 images.

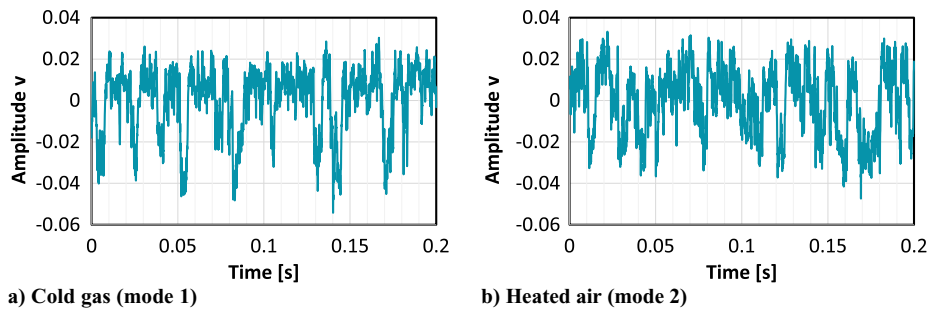a) Cold gas (mode 1)

b) Heated air (mode 2)

Fig. 22 Time histories of the switch mode between blunt and long penetration mode of the three-engine case.
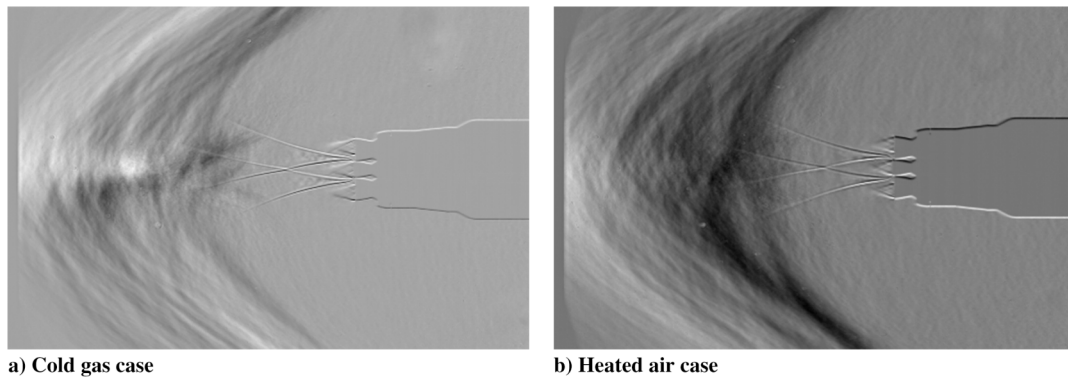

a) Cold gas case

b) Heated air case

Fig. 23 Average modal solution images of the three-engine case (mode 1 to mode 500)

experiments, unsteady pressure measurements in the supply air should be foreseen in those critical regions, such that these effects can be separated from the frequencies in the outer flowfield. The Strouhal number of 0.14 is more likely to come from outer flow interactions as it is close to the frequency of 0.126 measured in the cold gas single-engine case, where such frequency from the supply line were not observed, as the feed line does not show sharp edges.

The frequencies found in the pressure measurements cannot be observed in the PSD of the POD modes shown in Fig. 24. This is because the high-speed schlieren were recorded with 20 kHz, whereas the pressures were recorded with 50 kHz. Therefore, the frequencies of Strouhal numbers of 1.12, 1.16, and 1.16 are out of the measurement range of the schlieren recordings. For the lower dominant normalized frequencies of 0.056, 0.14, and 0.64, the reason could be that the schlieren setup was not sensitive enough to capture those fluctuations, even though the Strouhal number of 0.14 was found in the schlieren videos of the heated air case.

The frequencies observed here are in the range of Strouhal numbers reported in literature for similar configurations. In [46]

dominant frequencies were found in the first two POD modes of a single-engine plume, with the lowest normalized frequency close to 0.2 (which can be calculated from the data given in [46]). Chen et al. [48] reported Strouhal numbers of 0.252 and 1.506 for the forces on a similar configuration as in [46]. For near-wake flows in the base area of an ascending Ariane 5 configuration, it was found that Strouhal numbers of 0.2 can be critical for the actuators of the thrust vector control, which presumably led to the failure of the Ariane 5 ECA maiden flight [5,53]. In this context, especially the lower dominant Strouhal numbers found here for the descending configurations are not that far off of the critical value. Hence, these frequencies should be taken into account in the design phase of a reentering first stage to avoid critical loads to the actuators and the launcher structure.

Figure 27 shows the normalized root-mean-square surface pressure fluctuations in the two cold gas test cases. The normalized pressure fluctuations are approximately one order of magnitude smaller than in near-wake flows of ascending launcher configurations, which are between 0.01 and 0.06 for Mach numbers between 0.5 and 0.9 [52]. They are higher in the case with three active engines.
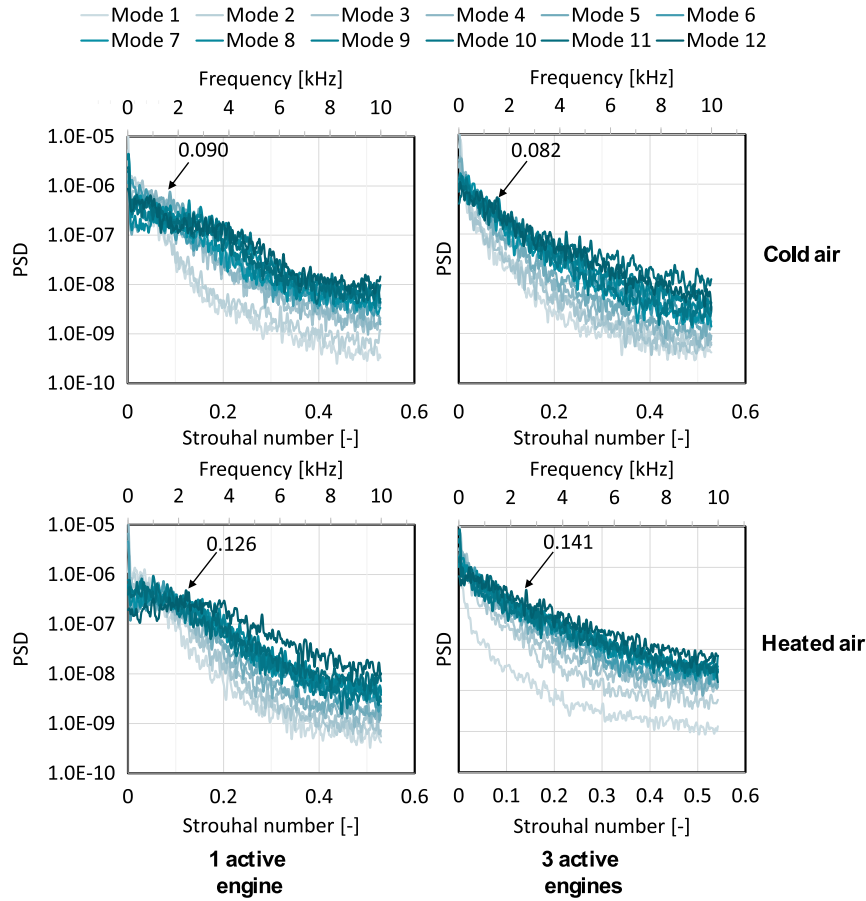
Fig. 24 PSD of the first 12 modes of the schlieren videos of the hypersonic retropropulsion cases.
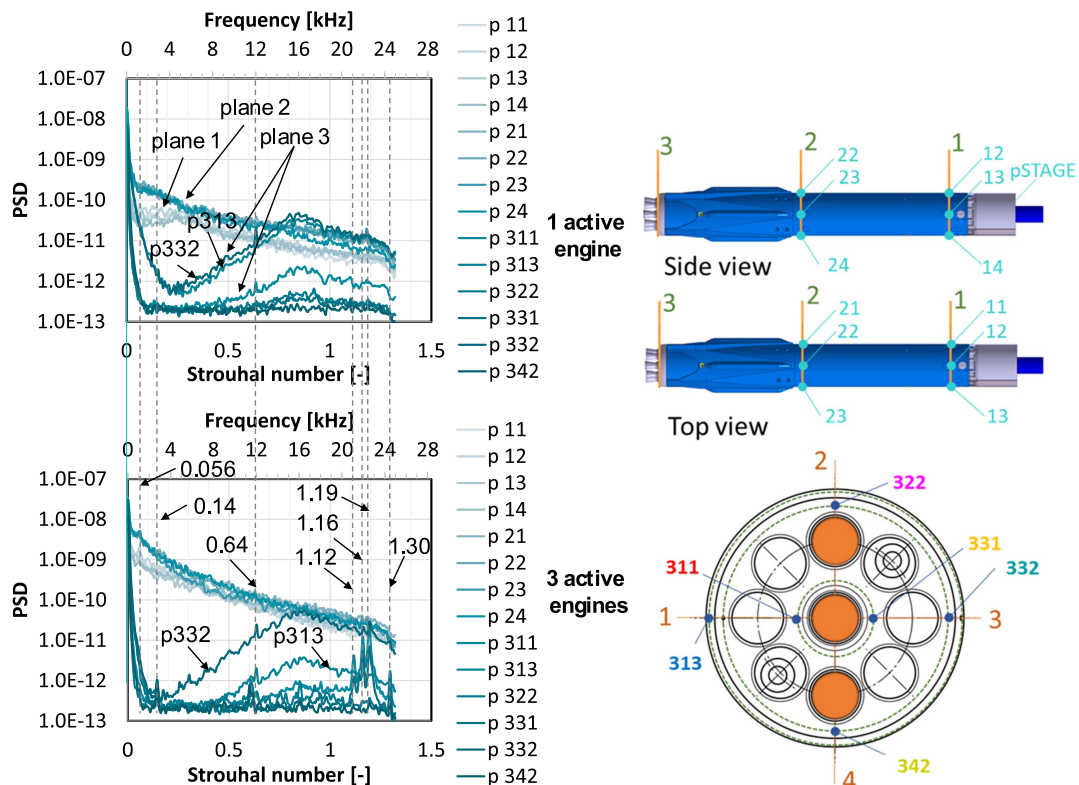
Fig. 25 PSD of the pressure measurements of the hypersonic retropropulsion cases.

a) Pressure sensor 311
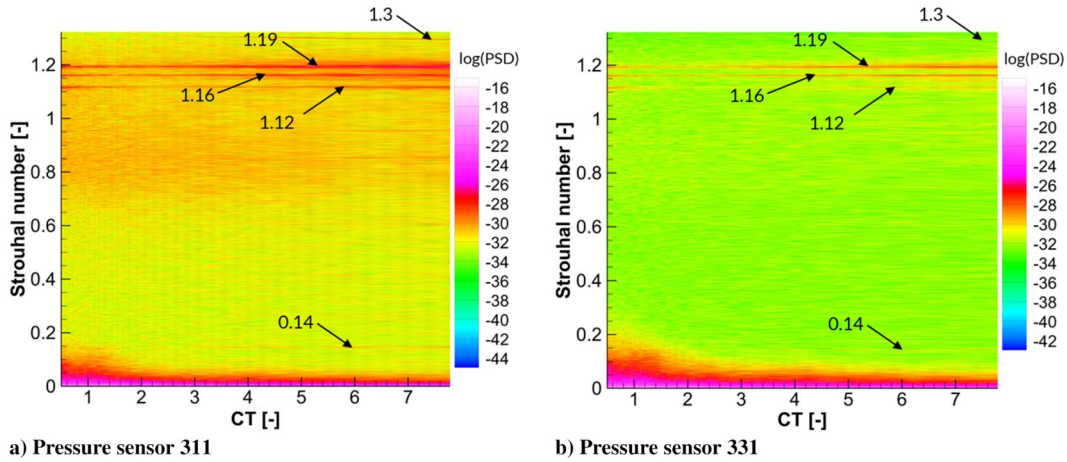
b) Pressure sensor 331

Fig. 26   Spectrograms of pressure measurements on the base area of RETALT1 versus the thrust coefficient, for the cold gas case with three active engines.
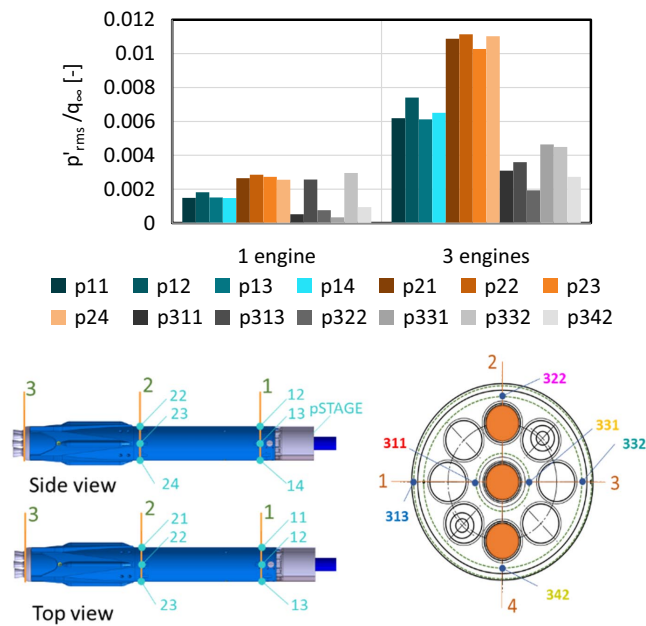

Fig. 27   Normalized rms surface pressure fluctuations in the two cold gas test cases with one and three active engines.

Presumably this is because the shielding of the plume is less effective in this case and the plume itself shows stronger unsteady behavior. Due to the shielding effect of the plume in both cases, the pressure fluctuations on the base area (plane 3) are smaller than downstream of the landing legs (plane 2) or on the cylindrical body (plane 1).

To close this section the absolute surface pressures for the single-engine configuration are shown in Fig. 28 and for the three-engine case in Fig. 29 for two Mach numbers, 5.29 (thin lines) and 7.04 (thick lines), at a Reynolds number of 2.36E+05. The thrust coefficients discussed in this paper in detail are marked with a dashed line. In Figs. 28a and 29a the pressure coefficients ($C_p = (p - p_\infty)/q_\infty$) are shown. In Figs. 28b and 29b the pressures are normalized with the total pressure behind the normal portion of the bow shock and, hence, with the total pressure in the stagnation point $p_{0,2}$. Korzun and Cassel [11] proposed the use of $p_e/p_{0,2}$ as similarity parameter for supersonic retropropulsion flows. Gutsche et al. [40] proposed to use $p_{0,2}$ for the normalization of the surface pressures. Indeed, it can be observed in Figs. 28 and 29 that for the pressures in the base area close to the plume (plane 3), a better similarity for different Mach numbers is achieved with the normalization with $p_{0,2}$. This also holds for the pressure in the wake area pSTAGE. For the pressures along the cylindrical body of the configuration (plane 1 and plane 2), the conventional pressure coefficients reach a better similarity.

VI.   Conclusions

In this work the unsteady flowfield of the hypersonic reentry burn of a descending first stage was discussed.

It was found for the case of a single active engine that the modes of the POD of the schlieren images mainly capture the unsteady fluctuation of the contact surface and the bow shock, probably caused by vortex rings emerging from the Mach disc. In the case of three active
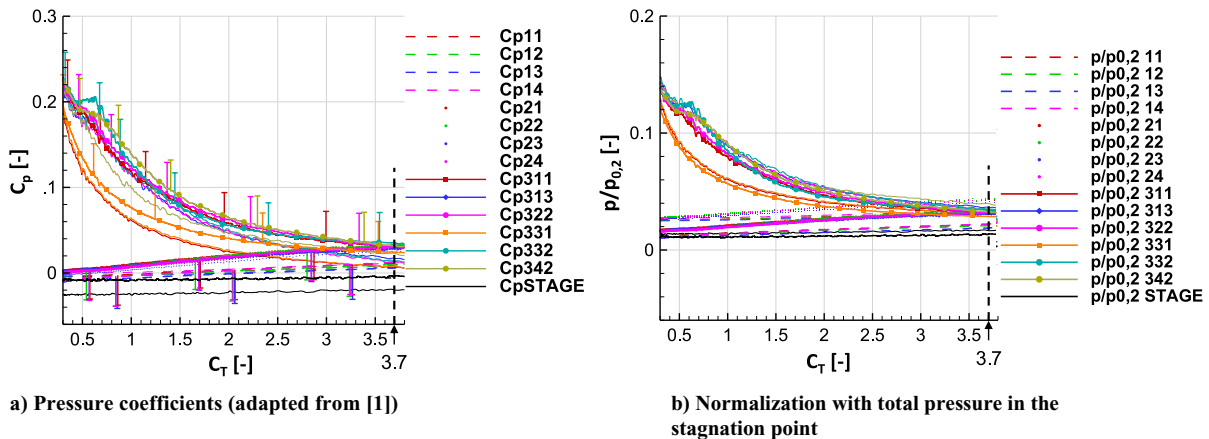

a) Pressure coefficients (adapted from [1])

b) Normalization with total pressure in the stagnation point

Fig. 28   Surface pressures for the single-engine case for $M_\infty = 5.29$ (thin lines) and $M_\infty = 7.04$ (thick lines).

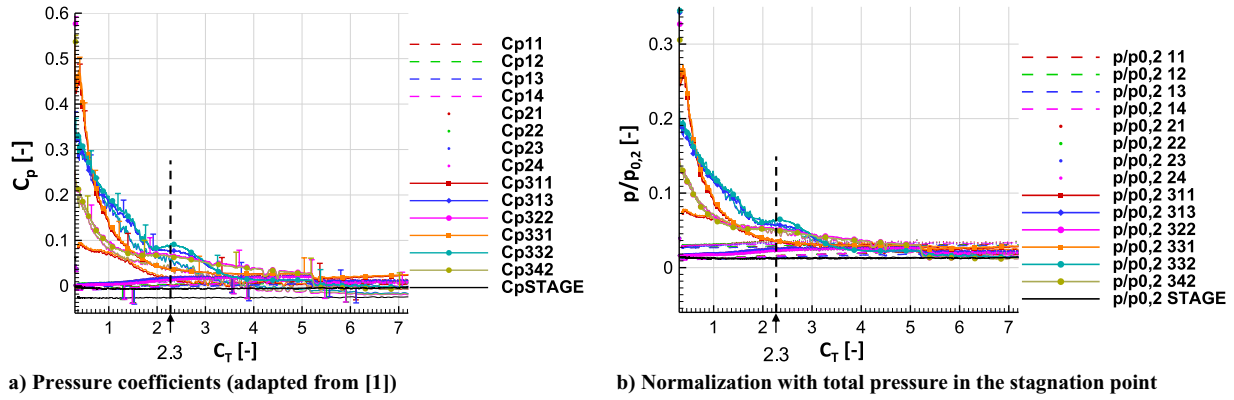a) Pressure coefficients (adapted from [1]) b) Normalization with total pressure in the stagnation point

Fig. 29 Surface pressures for the three-engine case for $M_\infty = 5.29$ (thin lines) and $M_\infty = 7.04$ (thick lines).

engines, the flowfield is dominated by the switch between the blunt and the long penetration mode.

Several dominant frequencies could be observed in the spectral analysis of the POD modes of the schlieren recordings for one and for three active engines. However, they are not very pronounced. In the frequency analysis of the pressure measurements, several dominant frequencies with Strouhal numbers around 0.1, 0.6, 1.1, and 1.3 could be observed. These were present in the three-engine case but absent in the single-engine case. A possible reason could be that the frequencies are specific for the three-engine case or that the frequencies come from a buffeting effect in the base area, which is shielded in the case of the single-engine case. Especially for the higher frequencies, also frequencies in the supply line of the model could be the reason for the frequencies in the pressures on the outer model surface. In future experiments, high-frequency pressure measurements should be implemented in the supply line to separate frequencies in the supply line from frequencies in the outer flowfield. The normalized root mean square pressure fluctuations are one order of magnitude smaller than for ascending launcher first stages and in the range of 0.002–0.012.

The scaling of the surface pressures with the total pressure downstream of the bow shock reaches good results for the base area and in the wake region, while along the cylindrical body of the launcher first stage, the conventional pressure coefficient reaches better similarity.

This work showed that the retropropulsion flowfield especially during the hypersonic reentry burn is highly complex and unsteady. It shows strongly varying modes. In the future, further efforts should be taken to better understand the effects of the unsteady flowfield on the launcher and its structures.

Acknowledgments

References

[1] Marwege, A., Kirchheck, D., Klevanski, J., and Gülhan, A., "Hypersonic Retro Propulsion for Reusable Launch Vehicles Tested in the H2K Wind Tunnel," *CEAS Space Journal*, Vol. 14, No. 3, 2022, pp. 473–499. https://doi.org/10.1007/s12567-022-00457-w

[2] Marwege, A., Hantz, C., Kirchheck, D., Klevanski, J., Vos, J., Laureti, M., Karl, S., and Gülhan, A., "Aerodynamic Phenomena of Retro Propulsion Descent and Landing Configurations," *2nd International Conference on Flight Vehicles, Aerothermodynamics and Re-Entry Missions and Engineering*, European Space Agency, 2022, Paper 2.13.02. https://doi.org/10.5281/zenodo.6783922

[3] Marwege, A., Hantz, C., Kirchheck, D., Klevanski, J., Gülhan, A., Charbonnier, D., and Vos, J., "Wind Tunnel Experiments of Interstage Segments Used for Aerodynamic Control of Retro-Propulsion Assisted Landing Vehicles," *CEAS Space Journal*, Vol. 14, No. 3, 2022, pp. 447–471. https://doi.org/10.1007/s12567-022-00425-4

Appendix: Tables of Surface Pressures and Normalized Surface Pressure Fluctuations

Table A1   Surface pressures of hypersonic retropropulsion tests in H2K presented in this paper

Run	p 11 [bar]	p 12 [bar]	p 13 [bar]	p 14 [bar]	p 21 [bar]	p 22 [bar]	p 23 [bar]	p 24 [bar]	p 311 [bar]	p 312 [bar]	p 313 [bar]	p 322 [bar]	p 331 [bar]	p 332 [bar]	p 333 [bar]	p 342 [bar]
90_5	0.00651	0.00646	0.00623	0.00674	0.00852	0.00878	0.00819	0.00862	0.00627	0.00839	0.00735	0.00695	0.00630	0.00698	0.00821	0.00796
93_7	0.00623	0.00597	0.00589	0.00655	0.00676	0.00661	0.00636	0.00668	0.00473	0.00616	0.00373	0.00339	0.00498	0.00370	0.00593	0.00358

Table A2   Normalized surface pressure fluctuations of hypersonic retropropulsion tests in H2K presented in this paper

Run	p'_{rms}/q_∞ 11	p'_{rms}/q_∞ 12	p'_{rms}/q_∞ 13	p'_{rms}/q_∞ 14	p'_{rms}/q_∞ 21	p'_{rms}/q_∞ 22	p'_{rms}/q_∞ 23	p'_{rms}/q_∞ 24	p'_{rms}/q_∞ 311	p'_{rms}/q_∞ 312	p'_{rms}/q_∞ 313	p'_{rms}/q_∞ 322	p'_{rms}/q_∞ 331	p'_{rms}/q_∞ 332	p'_{rms}/q_∞ 333	p'_{rms}/q_∞ 342
90_5	0.00148	0.00182	0.00152	0.00148	0.00264	0.00285	0.00273	0.00256	0.00053	0.00257	0.00077	0.00033	0.00296	0.00094	0.00148	0.00182
93_7	0.00618	0.00740	0.00612	0.00650	0.01087	0.01114	0.01027	0.01102	0.00310	0.00360	0.00193	0.00464	0.00449	0.00272	0.00618	0.00740

[4] Daub, D., Willems, S., and Gülhan, A., "Experiments on Aerothermoe-lastic Fluid–Structure Interaction in Hypersonic Flow," *Journal of Sound and Vibration*, Vol. 531, Aug. 2022, Paper 116714.
https://doi.org/10.1016/j.jsv.2021.116714

[5] Saile, D., and Gülhan, A., "Aeroacoustic Coupling Effect During the Ascent of Space Transportation Systems," *AIAA Journal*, Vol. 59, No. 7, 2021, pp. 2346–2356.
https://doi.org/10.2514/1.J059747

[6] Marwege, A., and Gülhan, A., "Aerodynamic Characteristics of the Retro Propulsion Landing Burn of Vertically Landing Launchers," *Journal of Spacecraft and Rockets* (in review).

[7] De Zaiacomo, G., Blanco Arnao, G., Bunt, R., and Bonetti, D., "Mission Engineering for the RETALT VTVL Launcher," *CEAS Space Journal*, Vol. 14, No. 3, 2022, pp. 533–549.
https://doi.org/10.1007/s12567-021-00415-y

[8] Marwege, A., Gülhan, A., Klevanski, J., Riehmer, J., Karl, S., Kirch-heck, D., Bonetti, D., Vos, J., Jevons, M., Krammer, A., and Carvalho, J., "Retro Propulsion Assisted Landing Technologies (RETALT): Current Status and Outlook of the EU Funded Project on Reusable Launch Vehicles," *70th International Astronautical Congress*, International Astronautical Federation Paper IAC-19.D2.4.5x49370, 2019.
https://doi.org/10.5281/zenodo.5770046

[9] Korzun, A. M., Braun, R. D., and Cruz, J. R., "Survey of Supersonic Retropropulsion Technology for Mars Entry, Descent, and Landing," *Journal of Spacecraft and Rockets*, Vol. 46, No. 5, 2009, pp. 929–937.
https://doi.org/10.2514/1.41161

[10] Edquist, K. T., Korzun, A. M., Kleb, W. L., Hawke, V., Rizk, Y. M., Olsen, M. E., and Canabal, F., "Model Design and Pre-Test CFD Analysis for a Supersonic Retropropulsion Wind Tunnel Test," *AIAA Scitech 2020 Forum*, AIAA Paper 2020-2230, 2020.
https://doi.org/10.2514/6.2020-2230

[11] Korzun, A. M., and Cassel, L. A., "Scaling and Similitude in Single Nozzle Supersonic Retropropulsion Aerodynamics Interference," *AIAA Scitech 2020 Forum*, AIAA Paper 2020-0039, 2020.
https://doi.org/10.2514/6.2020-0039

[12] Korzun, A. M., Nielsen, E., Walden, A., Jones, W., Carlson, J.-R., Moran, P., Henze, C., and Sandstrom, T., "Computational Investigation of Retropropulsion Operating Environments with a Massively Parallel Detached Eddy Simulation Approach," *ASCEND 2020*, AIAA Paper 2020-4228, 2020.
https://doi.org/10.2514/6.2020-4228

[13] Shafner, J., and Korzun, A. M., "Computational Analysis of a Multiple-Nozzle Supersonic Retropropulsion Configuration," *AIAA Aviation 2021 Forum*, AIAA Paper 2021-2556, 2021.
https://doi.org/10.2514/6.2021-2556

[14] Edquist, K. T., "Status of Mars Retropropulsion Testing in the Langley Unitary Plan Wind Tunnel," *AIAA Scitech 2022 Forum*, AIAA Paper 2022-0911, 2022.
https://doi.org/10.2514/6.2022-0911

[15] Edquist, K. T., Alter, S. J., Glass, C. E., Kleb, W. L., Korzun, A. M., Wood, W. A., Canabal, F., Childs, R., Halstrom, L. D., and Matsuno, K. V., "Computational Modeling of Mars Retropropulsion Concepts in the Langley Unitary Plan Wind Tunnel," *AIAA Scitech 2022 Forum*, AIAA Paper 2022-0912, 2022.
https://doi.org/10.2514/6.2022-0912

[16] Halstrom, L. D., Pulliam, T. H., Childs, R., and Stremel, P., "OVER-FLOW Analysis of Supersonic Retropropulsion Testing on a Blunt Mars Entry Vehicle Concept," *AIAA Scitech 2022 Forum*, AIAA Paper 2022-0914, 2022.
https://doi.org/10.2514/6.2022-0914

[17] Korzun, A. M., and Edquist, K. T., "Development Status of Powered Descent for High-Mass Mars, Descent, and Landing Systems," *2nd International Conference on Flight Vehicles, Aerothermodynamics and Re-Entry Missions and Engineering*, European Space Agency Paper 3.18.02, 2022.

[18] Korzun, A. M., Nastac, G., Walden, A., Nielsen, E. J., Jones, W. T., and Moran, P., "Application of a Detached Eddy Simulation Approach with Finite-Rate Chemistry to Mars-Relevant Retropropulsion Operating Environments," *AIAA Scitech 2022 Forum*, AIAA Paper 2022-2298, 2022.
https://doi.org/10.2514/6.2022-2298

[19] Matsuno, K., Childs, R., Pulliam, T. H., Stremel, P., and Garcia, J. A., "OVERFLOW Analysis of Supersonic Retropropulsion Testing on the CobraMRV Mars Entry Vehicle Concept," *AIAA Scitech 2022 Forum*, AIAA Paper 2022-0913, 2022.
https://doi.org/10.2514/6.2022-0913

[20] Nastac, G., Korzun, A. M., Walden, A., Nielsen, E. J., Jones, W. T., and Moran, P., "Computational Investigation of the Effect of Chemistry on Mars Supersonic Retropropulsion Environments," *AIAA Scitech 2022 Forum*, AIAA Paper 2022-2299, 2022.
https://doi.org/10.2514/6.2022-2299

[21] Korzun, A. M., and Braun, R. D., "Conceptual Modeling of Supersonic Retropropulsion Flow Interactions and Relationships to System Perform-ance," *Journal of Spacecraft and Rockets*, Vol. 50, No. 6, 2013, pp. 1121–1133.
https://doi.org/10.2514/1.A32464

[22] Cordell, C. E., and Braun, R. D., "Analytical Modeling of Supersonic Retropropulsion Plume Structures," *Journal of Spacecraft and Rockets*, Vol. 50, No. 4, 2013, pp. 763–770.
https://doi.org/10.2514/1.A32391

[23] Finley, P. J., "The Flow of a Jet from a Body Opposing a Supersonic Free Stream," *Journal of Fluid Mechanics*, Vol. 26, No. 2, 1966, pp. 337–368.
https://doi.org/10.1017/S0022112066001277

[24] Jarvinen, P. O., and Adams, R. H., "The Aerodynamic Characteristics of Large Angled Cones with Retrorockets," NASA CR-124720, 1970, https://ntrs.nasa.gov/citations/19720005324.

[25] Ecker, T., Ertl, M., Klevanski, J., Krummen, S., and Dumont, E., "Aerothermal Characterization of the CALLISTO Vehicle During Descent," *9th European Conference for Aeronautics and Aerospace Sciences (EUCASS)*, EUCASS Assoc. Paper 4680, 2022, https://elib.dlr.de/187034/.
https://doi.org/10.13009/EUCASS2022-4680

[26] Ecker, T., Zilker, F., Dumont, E., Karl, S., and Hannemann, K., "Aero-thermal Analysis of Reusable Launcher Systems During Retro-Propulsion Reentry and Landing," *Space Propulsion Conference 2018*, ESA and 3AF, Paper SP2018 00040, 2018, https://elib.dlr.de/120072/.

[27] Zilker, F., "Aerothermal Analysis of Re-Usable First Stage During Rocket Retro-Propulsion," Master Thesis, Universität Stuttgart, Institut für Thermodynamik der Luft- und Raumfahrt (ITLR), Stuttgart, Ger-many, 2018, https://elib.dlr.de/119265/.

[28] Vos, J., Charbonnier, D., Marwege, A., Hantz, C., and Guelhan, A., "CFD Simulations and Wind Tunnel Experiments for Re-Usable Launch Vehicles," *2nd International Conference on Flight Vehicles, Aerothermodynamics and Re-Entry Missions and Engineering*, European Space Agency Paper 2.13.03, 2022.
https://doi.org/10.5281/zenodo.6759393

[29] Vos, J., Charbonnier, D., Marwege, A., Guelhan, A., Laureti, M., and Karl, S., "Aerodynamic Investigations of a Vertical Landing Launcher Configuration by Means of Computational Fluid Dynamics and Wind Tunnel Tests," *AIAA Scitech 2022 Forum*, AIAA Paper 2022-1308, 2022.
https://doi.org/10.2514/6.2022-1308

[30] Laureti, M., Karl, S., Marwege, A., and Guelhan, A., "Aerothermal Databases and CFD Based Load Predictions," *2nd International Conference on Flight Vehicles, Aerothermodynamics and Re-Entry Missions and Engineering*, European Space Agency Paper 2.13.04, 2022.
https://doi.org/10.5281/zenodo.6759561

[31] Laureti, M., and Karl, S., "Aerothermal Databases and Load Predictions for Retro Propulsion-Assisted Launch Vehicles (RETALT)," *CEAS Space Journal*, Vol. 14, No. 3, 2022, pp. 501–515.
https://doi.org/10.1007/s12567-021-00413-0

[32] Charbonnier, D., Vos, J., Marwege, A., and Hantz, C., "Computational Fluid Dynamics Investigations of Aerodynamic Control Surfaces of a Vertical Landing Configuration," *CEAS Space Journal*, Vol. 14, No. 3, 2022, pp. 517–532.
https://doi.org/10.1007/s12567-022-00431-6

[33] Bouarfa, M., Bourgoing, A., Carrat, J.-M., Puech, D., Jubera, M., and Brenner, P., "CFD Retro-Propulsion Simulation with FLUSEPA Code," *2nd International Conference on Flight Vehicles, Aerothermodynamics and Re-Entry Missions and Engineering*, European Space Agency Paper 3.18.03, 2022.

[34] Scarlatella, G., Tajmar, M., and Bach, C., "Advanced Nozzle Concepts in Retro-Propulsion Applications for Reusable Launch Vehicle Recov-ery: A Case Study," *72nd International Astronautical Congress (IAC)*, International Astronautical Federation Paper IAC-21-D2.5.8, 2021.

[35] Scarlatella, G., Sieder-Katzmann, J., Roßberg, F., Weber, F., Mancera, C. T., Bianchi, D., Tajmar, M., and Bach, C., "Design and Development of a Cold-Flow Test-Bench for Study of Advanced Nozzles in Subsonic Counter-Flows," *Aerotecnica Missili & Spazio*, Vol. 101, No. 3, 2022, pp. 201–213.
https://doi.org/10.1007/s42496-022-00117-6

[36] Ghosh, D., and Gunasekaran, H., "Large Eddy Simulation (LES) of Aerospike Nozzle Assisted Supersonic Retro-Propulsion (SRP)," *AIAA Aviation 2021 Forum*, AIAA Paper 2021-2489, 2021.
https://doi.org/10.2514/6.2021-2489

[37] Mejia, N. A., and Schmidt, B. E., "Experimental Investigation of Flow Interaction Dynamics in Supersonic Retropropulsion," *Journal of Spacecraft and Rockets*, Vol. 59, No. 5, 2022, pp. 1753–1762.
https://doi.org/10.2514/1.A35228

[38] Huang, W., "A Survey of Drag and Heat Reduction in Supersonic Flows by a Counterflowing Jet and Its Combinations," *Journal of Zhejiang University—Science A*, Vol. 16, No. 7, 2015, pp. 551–561.
https://doi.org/10.1631/jzus.A1500021

[39] Venkatachari, B. S., Mullane, M., Cheng, G., and Chang, C.-L., "Numerical Study of Counterflowing Jet Effects on Supersonic Slender-Body Configurations," *33rd AIAA Applied Aerodynamics Conference*, AIAA Paper 2015-3010, 2015.
https://doi.org/10.2514/6.2015-3010

[40] Gutsche, K., Marwege, A., and Gülhan, A., "Similarity and Key Parameters of Retropropulsion Assisted Deceleration in Hypersonic Wind Tunnels," *Journal of Spacecraft and Rockets*, Vol. 58, No. 4, 2021, pp. 984–996.
https://doi.org/10.2514/1.A34910

[41] Jarvinen, P. O., and Hill, J. A. F., "Penetration of Retrorocket Exhausts into Subsonic Counterflows," *Journal of Spacecraft and Rockets*, Vol. 10, No. 1, 1973, pp. 85–86.
https://doi.org/10.2514/3.27737

[42] Daso, E. O., Pritchett, V. E., Wang, T.-S., Ota, D. K., Blankson, I. M., and Auslender, A. H., "Dynamics of Shock Dispersion and Interactions in Supersonic Freestreams with Counterflowing Jets," *AIAA Journal*, Vol. 47, No. 6, 2009, pp. 1313–1326.
https://doi.org/10.2514/1.30084

[43] Kirchheck, D., Marwege, A., Klevanski, J., and Gülhan, A., "Hypersonic Retrograde Propulsion Experiments–A Basis for Validation of CFD Within RETPRO," *9th European Conference for Aeronautics and Space Sciences (EUCASS)*, EUCASS Assoc. Paper 4435, 2022, https://elib.dlr.de/190741/.
https://doi.org/10.13009/EUCASS2022-4435

[44] Mc Ghee, R. J., "Effects of a Retronozzle Located at the Apex of a 140 deg Blunt Cone at Mach Numbers of 3.00, 4.50, and 6.00," NASA TN D-6002, 1971.

[45] Berry, S. A., Rhode, M. N., and Edquist, K., "Supersonic Retropropulsion Validation Experiment in the NASA Langley Unitary Plan Wind Tunnel," *Journal of Spacecraft and Rockets*, Vol. 51, No. 3, 2014, pp. 664–679.
https://doi.org/10.2514/1.A32649

[46] Bathel, B. F., Litzner, C. R., Jones, S. B., Berry, S. A., Smith, N. T., and Garbeff, T. J., II, "High-Speed Schlieren Analysis of Retropropulsion Jet in Mach 10 Flow," *Journal of Spacecraft and Rockets*, Vol. 57, No. 1, 2020, pp. 33–48.
https://doi.org/10.2514/1.A34522

[47] Montgomery, K. A., Bruce, P. J., and Navarro-Martinez, S., "Dynamics of Varying Thrust Coefficients for Supersonic Retropropulsion During Mars EDL," *AIAA Scitech 2022 Forum*, AIAA Paper 2022-0935, 2022.
https://doi.org/10.2514/6.2022-0935

[48] Chen, L.-W., Wang, G.-L., and Lu, X.-Y., "Numerical Investigation of a Jet from a Blunt Body Opposing a Supersonic Flow," *Journal of Fluid Mechanics*, Vol. 684, Oct. 2011, pp. 85–110.
https://doi.org/10.1017/jfm.2011.276

[49] Schauerhamer, D. G., Zarchi, K. A., Kleb, W. L., Carlson, J.-R., and Edquist, K. T., "Supersonic Retropropulsion Computational Fluid Dynamics Validation with Langley 4×4 Foot Test Data," *Journal of Spacecraft and Rockets*, Vol. 51, No. 3, 2014, pp. 693–714.
https://doi.org/10.2514/1.A32693

[50] Codoni, J. R., and Berry, S. A., "Supersonic Retropropulsion Dynamic Data Analysis from NASA Langley Unitary Plan Wind Tunnel," *Journal of Spacecraft and Rockets*, Vol. 51, No. 3, 2014, pp. 715–723.
https://doi.org/10.2514/1.A32619

[51] Niezgodka, F.-J., "Der Hyperschallwindkanal H2K des DLR in Köln-Porz (Stand 2000)," DLR, Cologne, Germany, 2001, https://elib.dlr.de/13874/.

[52] Saile, D., *Experimental Analysis on Near-Wake Flows of Space Transportation Systems*, Forschungsbericht, Vol. 4, Rheinisch-Westfälische Technische Hochschule Aachen (RWTH), Aachen, 2019, https://elib.dlr.de/130993/.

[53] Statnikov, V., Meinke, M., and Schröder, W., "Reduced-Order Analysis of Buffet Flow of Space Launchers," *Journal of Fluid Mechanics*, Vol. 815, March 2017, pp. 1–25.
https://doi.org/10.1017/jfm.2017.46

C. Bonnal
Associate Editor